ACS OMEGA

Open Access

http://pubs.acs.org/journal/acsodf

Article

Transforming Waste to Innovation: Sustainable Piezoelectric Properties of $Pb(Ti_{0.52}Zr_{0.48})O_3$ with Recycled β-PbO Massicot

Amna Idrees,◆ Gwangseop Lee,◆ Hamid Jabbar, Muhammad Siyar, Muhammad Zubair Khan, Farah Mumtaz, Aqeel Ahmad Taimoor, Awais Ahmad, Tauseef Ahmed, Jung-Hyuk Koh,* and Mohsin Saleem*

Cite This: *ACS Omega* 2025, 10, 38385−38396

Read Online

ACCESS | Metrics & More | Article Recommendations

ABSTRACT: In this study, we present an indigenous approach to enhancing the properties of $Pb(Zr_{0.52}Ti_{0.48})O_3$ by synthesizing it from β-PbO obtained from spent lead-acid batteries. Initially, β-PbO, orthorhombic massicot, was produced by two-step heating, and 99.9% lead powder was derived from recovered lead-acid batteries at 700 °C. The synthesized β-PbO was thoroughly analyzed using X-ray diffraction, field emission scanning electron microscopy, Fourier-transform infrared spectroscopy, X-ray photoelectron spectroscopy, and Raman spectroscopy. Subsequently, the β-PbO precursor was utilized for the synthesis of PZT, offering a cost-effective alternative. The morphology of the sintered sample revealed the formation of homogeneous and uniform grains, indicative of significant densification (∼99%) of the ceramic. The sintered PZT exhibited an enhanced piezoelectric coefficient (d_{33}) of 270 pC/N, a Q_m factor of 30.94, and a dielectric constant of 1590 at ∼10 kHz. This study highlights the feasibility of using β-PbO derived from recycled lead ingots to synthesize materials, presenting a sustainable approach that contributes to technological progress and environmental conservation.

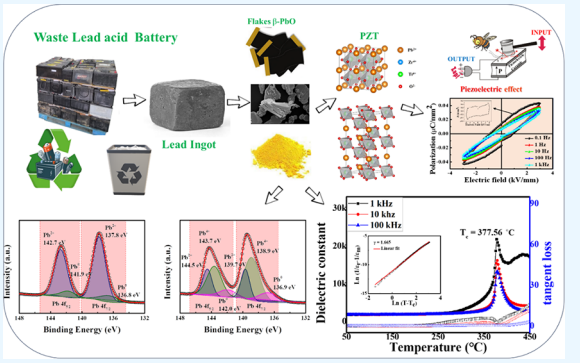

1. INTRODUCTION

The escalation of industrialization and surging energy requirements has brought forth a series of pressing environmental issues that demand urgent attention. Environmental degradation resulting from conventional fossil fuels and the inadvertent pollution of soil and water from purportedly green alternatives such as batteries, supercapacitors, and smart electronics supported by piezoelectric materials have garnered widespread concern.[1−3] Effective resource conservation strategies are imperative to mitigate the environmental impact associated with sophisticated technologies reliant on advanced materials like piezoelectric materials, and pyroelectric materials used in sensors, actuators, transducers, and nanogenerators.[4,5]

Over the past few decades, there has been a significant evolution in consumer electronics. Piezoelectric materials, owing to their distinctive electromechanical properties, have garnered considerable attention across various applications. These materials possess the capability to convert mechanical stress into electrical signals, as well as to convert electrical energy into mechanical tension. Furthermore, the application of an electric field can induce strain within these materials, while external mechanical stress can lead to material polarization. This phenomenon finds diverse applications, including in electrical sensors and specific actuators. Examples of such applications encompass electronic fuel injectors, automotive airbag sensors, accelerometers, gyroscopes, magnetometers, camera zoom mechanisms and autofocus systems in smartphones and cameras.[6−8]

In noncentrosymmetric unit cells, the manifestation of the piezoelectric effect is intimately linked to the absence of charge symmetry at the center of the unit cell. This lack of charge symmetry distinguishes them from their centrosymmetric counterparts. Within the realm of crystallography, such unit cells are classified into 21 crystal classes that lack a center of symmetry.[9] Remarkably, with the exception of one class, all these exhibit inherent piezoelectric characteristics. Perovskite structures, notably, have emerged as commercially accessible piezoelectric materials, frequently comprising solid solutions like $PbTiO_3$. Above its Curie temperature (T_c), $PbTiO_3$ adopts a nonpiezoelectric cubic unit cell configuration.[10] However, upon cooling below its T_c, a structural phase transition occurs,

Received: January 3, 2025
Revised: August 5, 2025
Accepted: August 12, 2025
Published: August 21, 2025

Table 1. Composition of Different Elements in Refined Lead Ingot

Elements	Pb	Bi	Ag	Fe	Zn	Cd	Ca	Al	S
Conc %	99.98	0.012	0.00119	0.00015	0.00019	0.00001	0.000012	0.00007	0.00023
Elements	**Sn**	**As**	**Cu**	**Sb**	**Se**	**Ni**	**Te**	**P**	
Conc %	0.0001	0.00005	0.00064	0.00016	0.00020	0.00016	0.00017	0.00030	

transforming the material from cubic to tetragonal symmetry, thereby inducing spontaneous polarization. This phenomenon underscores the pivotal role of structural dynamics in dictating the piezoelectric behavior of materials.[11]

The coexistence of phases near the MPB, materials often exhibit their enrichment in piezoelectric capabilities. At the rhombohedral/tetragonal phase region, where titanium Ti is present in a 0.48 molar ratio, has been demonstrated to enhance the piezoelectric effect. Furthermore, incorporating dopants into an MPB composition creates ceramics with excellent piezoelectric properties.[12−14] These material's composition at MPB has good electromechanical characteristics, making them strong candidates for use as lead piezoelectric materials.[15] Lead-free piezoelectric materials often exhibit temperature-dependent phase boundaries that lead to insufficient piezoelectric properties, posing challenges for the production of lead-free materials. Achieving genuine MPB is crucial for attaining high performance and stability in these materials. Strengthening the temperature stability of their electrical characteristics is imperative to address this issue effectively. The compositions near MBP have extraordinary electromechanical properties. However, there is increasing concern over the reuse and disposal of lead-containing devices due to their toxicity.[16] Due to lead's potential to evaporate during manufacturing and persist in the environment, stricter regulations have been imposed by many nations. Despite this, the remarkable piezoelectric properties of PZTs remain invaluable, enabling crucial applications like medical imaging, which plays a pivotal role in accurate diagnosis and potentially saving lives.[17]

Lead zirconate ($PbZrO_3$) lacks piezoelectric properties due to its antiferroelectric nature. Similarly, pure $PbTiO_3$ has limited utility as a piezoelectric material. However, the solid solution $Pb(Zr_{1-x}Ti_x)O_3$ exhibits exceptional piezoelectric characteristics.[18] On-going proposals for modifications to its composition−temperature phase diagram indicate the current exploration of its complex nature, even five decades after its discovery, emphasizing the intricate complexity of PZT and related ferroelectric materials.[19,20]

Several techniques,[19,20] including solid-state reaction,[21,22] semiwet approach,[23,24] molecular precursor pathway, oxide coprecipitation sol−gel,[25] mechanochemical synthesis, hydrothermal process,[26] and spray drying[27] have been used to create PZT ceramic powders. PbO, TiO_2, and ZrO_2 are frequently used as precursors in solid-state reactions to produce PZT. The reactions' sequences are now well characterized, with multiple studies providing detailed descriptions.

In the 1970s and 1980s, energy and environmental challenges were largely overlooked, but their significance emerged in the 1990s, expanding significantly in the 2000s and 2010s. Notably, research areas addressing these issues experienced substantial growth, with topics related to energy and the environment contributing to over 50% of the increased publication output on piezoelectric materials in the 2010s.[26]

Despite advancements, the development of piezoelectric materials continues to face challenges such as excessive consumption of high energy and lower ecological compatibility in contract compared to other electronic materials.[27−35] The development of piezoelectric materials confronts challenges such as excessive energy consumption and lower environmental friendliness when compared to other electronic materials. Conversely, the inadequate recycling of spent piezoelectric materials contributes significantly to the ecological footprint of the piezoelectric industry. Therefore, there is an urgent necessity for efficient recycling methodologies that afford discarded piezo materials in the form of precursors a second lease of life at minimal energy expense, thereby reducing both energy consumption and environmental impact before their ultimate disposal.[36]

There is little to no substantial research evidence available in the recycling of toxic materials employed for the synthesis of piezoelectric materials from spent lead-acid batteries. According to our knowledge, the utilization of lead oxide sourced from lead acid batteries in PZT synthesis has not been previously documented. Exploration of the production of nanosized alpha and beta forms of PbO particles via the decomposition of lead citrate has been previously synthesized. These particles were then successfully incorporated into lead-acid battery paste as a precursor material. Their study highlighted the significant influence of oxygen presence in the synthesis medium on particle size and crystal structure.[37] Utilizing a sonochemical technique, a Pb(II) coordination polymer was synthesized, yielding pure alpha-lead oxide (α-PbO) nanoparticles with an average size of 70 nm. This study prompts inquiry into the recyclability of lead oxide derived from lead ingots, offering significant environmental benefits and enhancing the production of lead-based devices.[38] The method not only conserves energy and reduces toxic gas emissions but also yields exceptionally pure, desirable, and high-performance lead oxide at a reduced cost.[39]

This study focuses on formulating PZT powder comprising $Pb(Zr_{0.52}Ti_{0.48})O_3$ using a PbO precursor derived from recycled lead acid batteries. Investigating synthesis mechanisms of lead oxides in ambient atmospheric conditions was conducted. The study investigates into analyzing the microstructure and piezoelectric properties, as well as examining the structural characteristics of the synthesized materials. Additionally, electromechanical testing of the ceramic material was explored to further understand its performance.

2. EXPERIMENTAL SECTION

2.1. Materials. Lead oxide (PbO) has two crystal forms: red tetragonal (α-PbO) and yellow orthorhombic (β-PbO). α-PbO is formed at lower temperatures, whereas β-PbO is produced at temperatures above 486 °C. The synthesis of PbO was carried out utilizing a lead ingot 99.9% pure from a recovered lead acid battery. To synthesize $Pb(Zr_{0.52}Ti_{0.48})O_3$, β-PbO (yellow color) was combined with TiO_2 (>99% purity, Aldrich Chemical) and ZrO_2 as starting materials.

2.2. Synthesis of Lead Oxide. The lead ingot from spent lead-acid batteries was crushed into lead powder. Table 1 shows composition of different elements in lead ingot. To

https://doi.org/10.1021/acsomega.5c00071
ACS Omega 2025, 10, 38385−38396

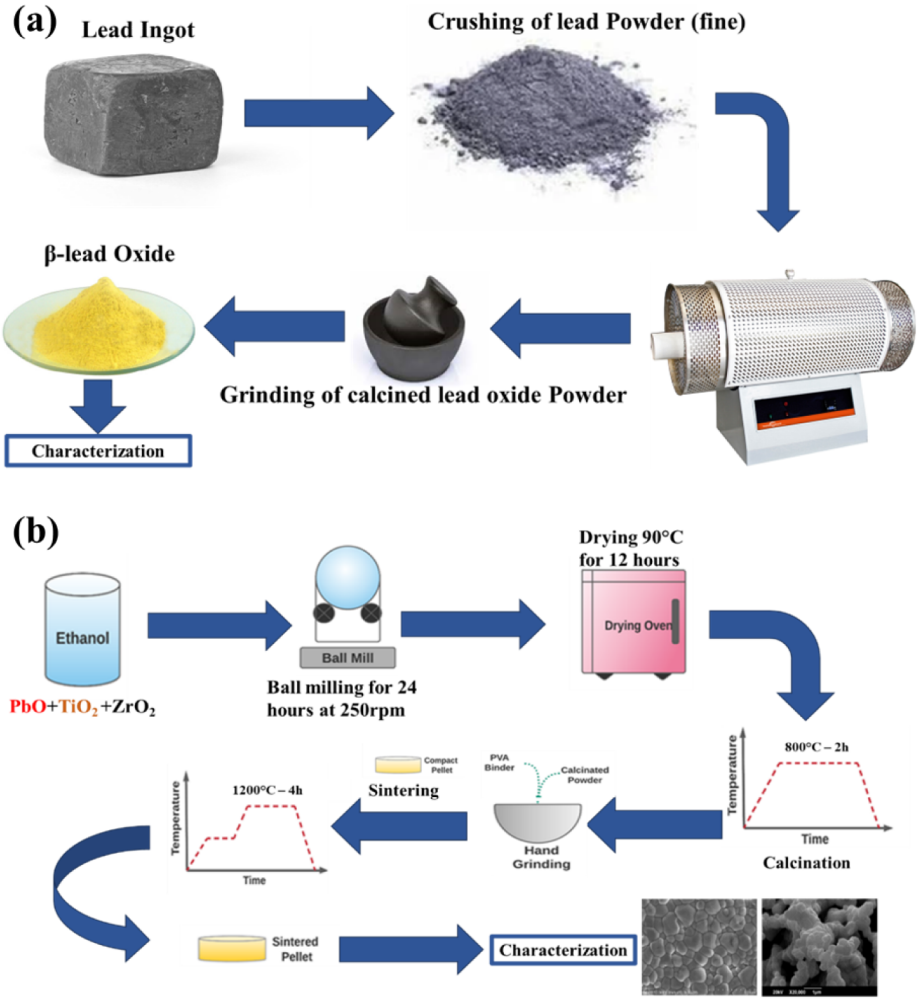

Figure 1. Synthesis of lead oxide (PbO) nanopowder (a); schematic of the experimental procedure of PZT (b).

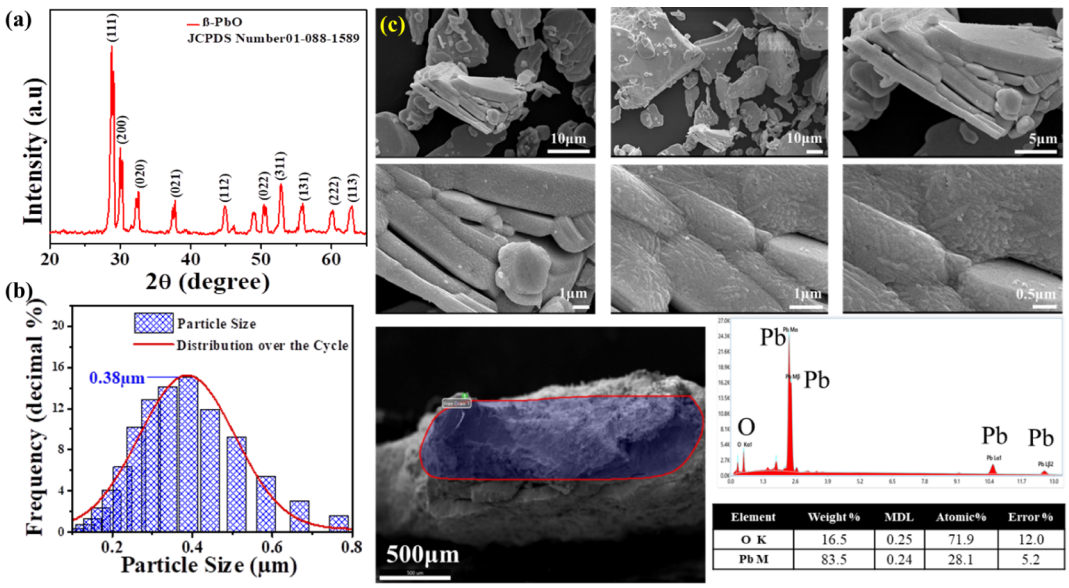

Figure 2. XRD pattern of β-PbO synthesized at 700 °C (a). Particle size distribution of lead oxide (β-PbO) synthesized at 700 °C (b). SEM and EDX images of the β-PbO powders (c).

synthesize lead oxide β-PbO, lead (Pb) powder was calcined in two steps in a tube furnace at 700 °C for 6 h illustrated in Figure 1(a).

2.3. Synthesis of PZT. Utilizing a solid-state method, reagent-grade oxides were used to create the piezoelectric ceramic. β-PbO from recycled Pb from batteries was mixed

https://doi.org/10.1021/acsomega.5c00071
ACS Omega 2025, 10, 38385−38396

with precursors TiO_2 and ZrO_2 to produce $Pb(Zr_{0.52}Ti_{0.48})O_3$ i.e., PZT. The oxide mixture was milled with ethanol for 24 h. The resulting slurry was dried in a drying oven at 90 °C for 12 h. The powder was calcined at a temperature of 800 °C for 2 h at 5 °C/min. The calcined powder was milled with ethanol for 12 h. The resulting mixture was dried in a drying oven at 90 °C for 12 h. The powder was mixed with 20% PVA binder and pressed into a pellet, of a diameter of 12 mm, by applying 3 tons of pressure (Uniaxial Press). The pellets were sintered at a temperature of 1200 °C for 4 h at 5 °C/min. Figure 1b represents the schematic of synthesis and sintering of PZT.

2.4. Characterization. X-Ray diffraction (XRD) analysis for PbO and PZT was conducted over the 20° to 80° range using a STOE diffractometer. Structural parameters were determined through Rietveld refinement of the powder patterns, utilizing CASAS software, while refined crystal structures were visualized with VESTA software. Microstructural details were examined via a JEOL JSM-6490LAM Scanning Electron Microscope. Raman spectroscopy was performed with an i-RAMAN setup at a 40 mW laser power, covering the spectral range of k = 150−4000 cm^{-1}. FTIR spectra for both samples were recorded using a PerkinElmer (Spectrum 100) instrument. Thermal analysis, including TGA and DSC, was conducted with TA's SDT650 system. Particle size distribution was assessed with a laser particle size analyzer Horiba LA-920. Dielectric and electrical properties of the PZT materials were measured with an Agilent LCR meter. X-ray photoelectron spectroscopy (XPS) measurements were obtained using Thermo Fisher Scientific's k-alpha$^+$ system. Finally, the Polarization vs Electric Field characteristics were recorded using a Radiant Precision HVI-SC Analyzer.

3. RESULTS AND DISCUSSION

3.1. Structural Analysis and Particle Size Determination of β-PbO. Figure 2a demonstrates the XRD pattern of high-temperature synthesis of lead oxide massicot β-PbO at 700 °C. The major diffraction peaks (111), (200), (020), (021), (112), and other peaks are the characteristic peaks for

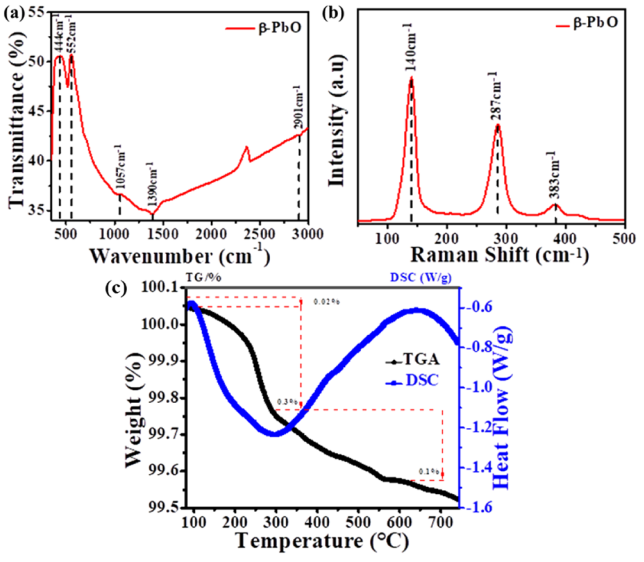

Figure 3. FTIR pattern of β-PbO (a); Raman spectra of β-PbO powder (b). Thermogravimetric analysis (TGA) and differential scanning calorimetry (DSC) of β-PbO powder (c).

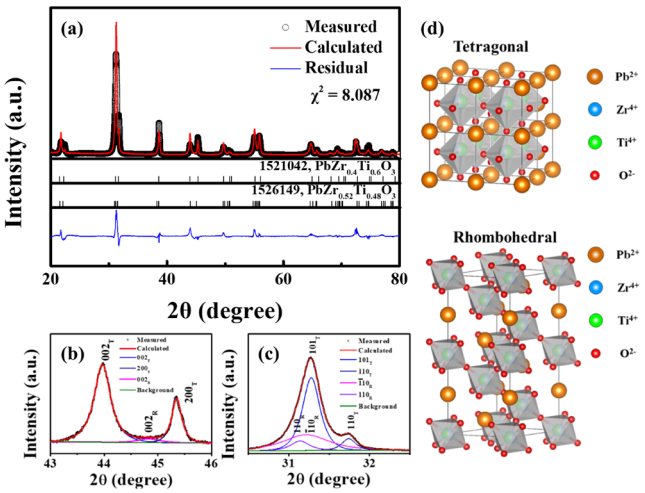

Figure 4. (a) XRD pattern of PZT. (b and c) Representative Rietveld fits to room temperature XRD patterns of polycrystalline PZT samples. The experimental, calculated, and varied patterns are shown by black dots, red solid lines, and pink solid lines, respectively. Bragg peaks' locations are depicted as solid bars. (d) Schematics of the crystal structure of PZT showing the arrangement of Pb^{2+}, Zr^{4+}, Ti^{4+}, and O^{2-} ions.

the orthorhombic phase of the β-PbO massicot that perfectly befits JCPDS # 01−088−1589, and show an orthorhombic phase structure.[40] No litharge (α-PbO) was observed which means that the phase of massicot was predominant in the PbO powder was massicot. No additional peaks were observed that could indicate the intermediate phase, such as lead(II) oxide hydrates ($3PbO{\cdot}H_2O$). The sharp and intense peaks associated with β-PbO suggest that the material has achieved excellent crystallinity. In the β-PbO unit cell, two lead sublayers are positioned with two oxygen sublayers, forming staggered Pb−O chains with lead atoms in an asymmetric square pyramidal coordination. The orthogonal lattice structure of massicot, a naturally occurring mineral form of lead(II) oxide, has the lattice parameters of a = 5.4921 Å, b = 5.8931 Å, and c = 4.7553 Å.[41] The particle size of the β-PbO was estimated using Debye−Scherer method. The particle sizes were determined as 0.5−2 μm.

Figure 2b depicts the size distribution plot for beta lead oxide (β-PbO) particles measured using a laser particle size analyzer. It shows that the particles had an average diameter of 0.38 μm. These results are quite close to those obtained from the XRD measurements. Figure 2c shows electron microscopic pictures and EDX, indicating the production of β-PbO flakes. By using Image J software on SEM images, it shows 2D β-PbO flakes with micron-sized widths. The thickness is less than 2 μm and the breadth spans from tens to several hundred micrometers. These agglomerates were made from numerous sheet-shaped particles with varying sizes and morphologies. The agglomeration phenomena might be attributed to the high condensation temperature and heat created during the impact and amalgamation processes in the development stage.[42] The composition of β-PbO was determined using the EDX method, showing the presence of lead (Pb) and oxygen (O).

3.2. Thermal Stability Analysis of β-PbO Using TGA and DSC. The FTIR was explored for the chemical bond and multiple strong bands in the 3000−450 cm^{-1} range in Figure 3a, which are likely due to the metal−oxygen vibrations (possibly Pb−O) in ceramic samples, with distinct bands

https://doi.org/10.1021/acsomega.5c00071
ACS Omega 2025, 10, 38385−38396

Table 2. Structural Parameters Obtained from Rietveld Refinements of XRD Data of $PbZr_xTi_{1-x}O_3$ at Room Temperature

	101		002						
	center peak		center peak		R_{wp}	χ^2	a	c	α
Tetragonal	101_T	31.2785	002_T	43.9663	3.3104	1.5708	3.9958	4.1153	90
	110_T	31.7434	200_T	45.3523					
Rhombohedral	110_R	31.1398	002_R	44.8133			4.08393	4.0839	89.60
	110_R	31.2133							
Average particle size	5.313 μm		6.206 μm						

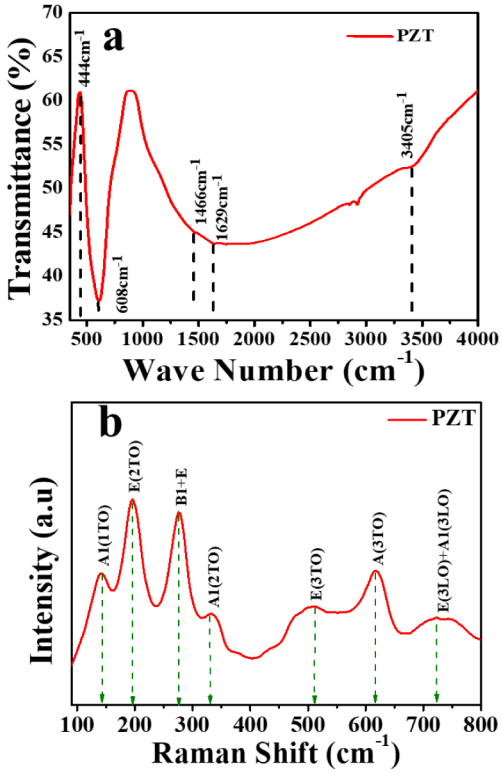

Figure 5. (a) FTIR spectra after calcination PZT. (b) Raman spectra of massicot (β-PbO) and PZT.

observed at 444, 552, 1054, 1393, 2901 cm^{-1}. The FTIR spectra show two prominent peaks at 466.74 cm^{-1} and 557.39 cm^{-1}, indicating the presence of lead and oxide.[43] The emergence of the transmission peak at 444 cm^{-1} denotes the presence of the (Pb−O) stretching vibration mode, whereas the transmission peak at 1057.03 cm^{-1} is associated with the (C═O). The stretching vibration modes represent a minimal influence of CO_2 suspension from air containment, respectively. The second peak at 1390 cm^{-1} represents the stretching vibration of the Pb−O Figure 3a.[44]

The vibrational properties of the synthesized beta lead oxide were studied using Raman spectroscopy. The Raman spectra were recorded in the range of 50 cm^{-1} to 500 cm^{-1}. The Pb-related crystal exhibits faint Raman bands near 65 cm^{-1} to 85 cm^{-1}, although they are not present in every tested region. In orthorhombic β-PbO, the first mode is triggered, resulting in a sharp absorption band at 140 cm^{-1}, which corresponds to the antisymmetric stretching vibration. The Pb-related materials frequently exhibit substantial stretching bands (due mostly to Pb−O). As Pb-related materials do not exhibit significant bands above 700 cm^{-1}, fundamental vibration bands are absent in this region. Figure 3b shows that the prominent band at 140 cm^{-1} indicates the presence of β-PbO massicot phase. The obtained spectra are also compatible with previous massicot spectra reported in the literature.[45]

In order to investigate thermal stability, the β-PbO sample was tested by TGA and DSC up to 720 °C at a heating rate of 10 °C/min, as presented in Figure 3c. Clearly, the synthesized PbO powder is highly stable up to 120 °C. Thermo-decomposition started at approximately 120 °C and passed through a maximum degradation at approximately 230 °C. The weight loss was very small, about 0.3%, thereby indicating the transformation of lead oxalate into lead oxide.[46] It is expected because in thermal decomposition, the lead does not go with any change in its oxidation state. In this way, the formation of lead oxide is already realized at the relatively low temperature of 500 °C. The DSC curve in Figure 3 clearly states that β-PbO is stable up to 120 °C discussed above, and then water molecules are released due to coordination. This has caused an endothermic peak at 123 °C with a heat enthalpy of 0.193 J/g. The two exothermic peaks can be seen, indicating that the material is releasing heat to maintain the same temperature as its reference material. The sample's DSC analytical result indicates a melting point of 320.7 °C, consistent with the β-PbO powder.[44,47]

3.3. Exploring the Morphotropic Phase Boundary in PZT. Figure 4a shows XRD patterns of PZT ceramic for the 2θ range of 20°−80°. The ceramic has a pristine perovskite structure with no evidence of any secondary phase. The diffraction peaks of PZT have been indexed using the standard JCPDS card (No. 01-088-1589) and (No. 00-033-0784). A strong reflection (110) occurs at 31.14°, which is quite similar to the value reported in the literature for the pure PZT ceramic phase.[48,49] It is owing to high crystallite development caused by the lowest energy at (110). The (111), (002) and (201) patterns correspond to the tetragonal phase. Figure 4b is an expanded 2θ range of 43°−46°, and it reveals that the composition is positioned at the MPB between R and T phases. A broad and overlapping peak has deconvoluted three peaks: a peak at position (002), followed by a peak of T phase at position (200), and a peak of R phase at position (200), by multipeak Gaussian−Lorentzian fitting. While Figure 4c is a zoom onto a restricted 2θ range, from 30.5° to 32.5°, a multipeak Gaussian−Lorentzian fit could give fine resolution to the broad overlapping peak and resolve it into four peaks formed by the (110) and (101) peaks of the T phase and by the (110 and 1−10) peaks of the R phase.[48,49] In Figure 4d, a unit cells are shown schematically as tetragonal ($P4mm$) and rhombohedral ($R3m$). The structural characteristics of room temperature XRD patterns were derived using Rietveld refinements. In Table 1, the optimized structural characteristics are provided. Table 2 shows the structural parameters of $PbZr_xTi_{1-x}O_3$ at room temperature obtained from Rietveld refinements of XRD data.

Figure 5a shows the FTIR spectrum of the PZT ceramic. Using a Fourier transform infrared (FTIR) spectroscope,

https://doi.org/10.1021/acsomega.5c00071
ACS Omega 2025, 10, 38385−38396

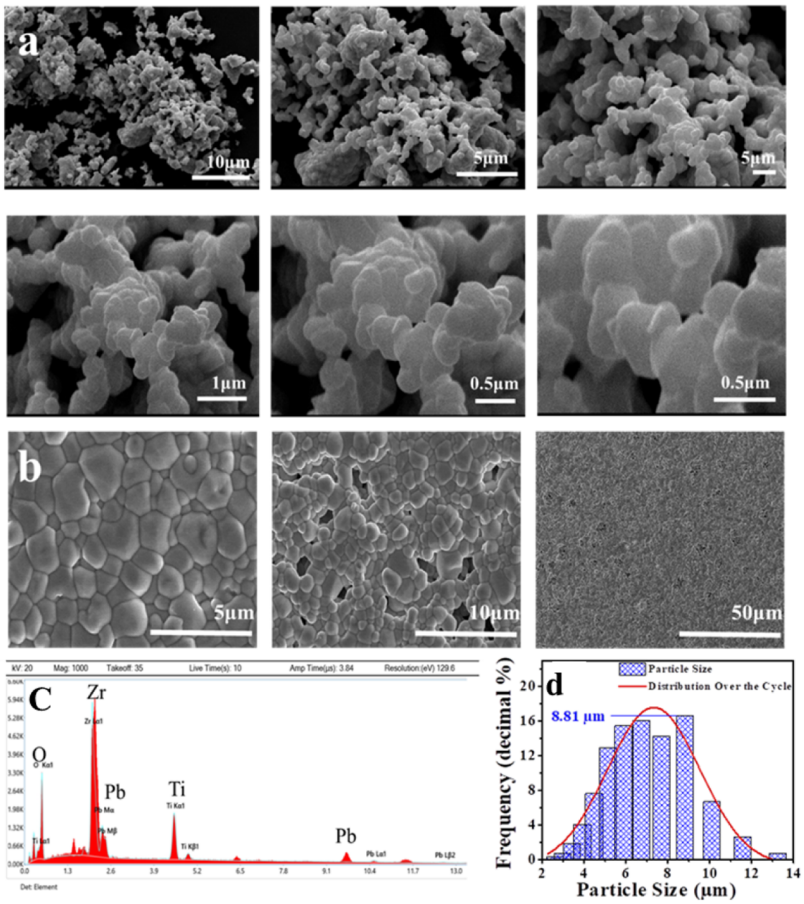

Figure 6. SEM images of pure PZT ceramic and sintered pellet (a, b) along with the EDS analysis of PZT ceramic (c). Particle size distribution of PZT (d).

molecular structures in the solid phase were examined between 400 cm^{-1} and 4000 cm^{-1}. The O−H groups' stretching vibration is caused by their hydrogen bonding to vibrate at a broad absorption band of 3405 cm^{-1}. The peaks at the 1629 cm^{-1} and 1406 cm^{-1} bands relate to the symmetric and asymmetric stretching vibration of −COO groups, respectively. The peak at ∼608 cm^{-1} is present which is attributed to Zr/Ti octahedral vibrations. This confirmed the formation of the tetragonal phase of PZT.[50]

Figure 5b shows the Raman spectra of PZT using a 532 nm laser source. The spectra can conveniently be divided into two frequency regions: namely, the Slater band in the frequency range of 100−400 cm^{-1} and the Ax band between 400 and 800 cm^{-1}. It is assigned to coupled oscillations of Zr/Ti within the O_6 framework while the Ax band is related to the bending motions of the oxygen octahedra. At first glance, the spectra are similar and identical to those described in previous literature.[50] The significant Raman peaks at 138, 197, 285, 334, 544, 606, and 718 cm^{-1} are assigned to the tetragonal PZT phase.[51,52] The modes between 150 cm^{-1}-350 cm^{-1} are due to A-site and B−O vibrations. The modes (E(3TO) and A1(3TO)) represents BO_6 octahedral vibrations. The A1(2TO) mode, appearing around ∼340 cm^{-1}, serves as a valuable indicator for tracking the structural properties of the PZT (lead zirconate titanate) system. This vibrational mode reflects the motion of Zr/Ti atoms along the *c*-axis, in an antiphase relationship with Pb and O atoms. This behavior signifies the coexistence of tetragonal and rhombohedral phases, distinguishing these from other ferroelectric phase configurations. Furthermore, the existence of mode B1 + E near ∼285 cm^{-1} without any splitting indicates the lack of a monoclinic phase, which would split the peak into two halves. These additional modes, the intensities of A1(1TO), E(2TO), and other modes with lower intensities, act as direct evidence for the existence of tetragonal and rhombohedral structures in PZT ceramics. In these modes, Zr/Ti atoms and the apical oxygen vibrate along the a- or *b*-axis, whereas the equatorial oxygen and Pb atoms exhibit motion in the opposite direction.[50]

The lead zirconate titanate (PZT) particle size and size distribution plot, as depicted in Figure 6d, were also measured using a laser particle size analyzer. The average diameter of the particles was 8.81 μm. Powders produced using this approach were analyzed based on particle size distribution. This investigation indicates that roughly 64% of particle sizes vary from 5 to 10 μm, 16% from 2 to 4 μm, and 20% from 11 to 14 μm at calcination temperatures of 700 °C, respectively. However, the particles were agglomerated as shown in FE-SEM (see Figure 6a, b), so the size range obtained is associated with the agglomeration rather than the isolated particles.

Figure 6b demonstrates that the microstructure analysis of sintered pellet (cross-section) was done using FE-SEM. The PZT powder images are shown having spherical particles with dimensions ranging from 0.5 to 5 μm. It was observed, that the particles are well dispersed and uniformly distributed with no agglomeration.[53] In Figure 6, the micrographs reveal a

https://doi.org/10.1021/acsomega.5c00071
ACS Omega 2025, 10, 38385−38396

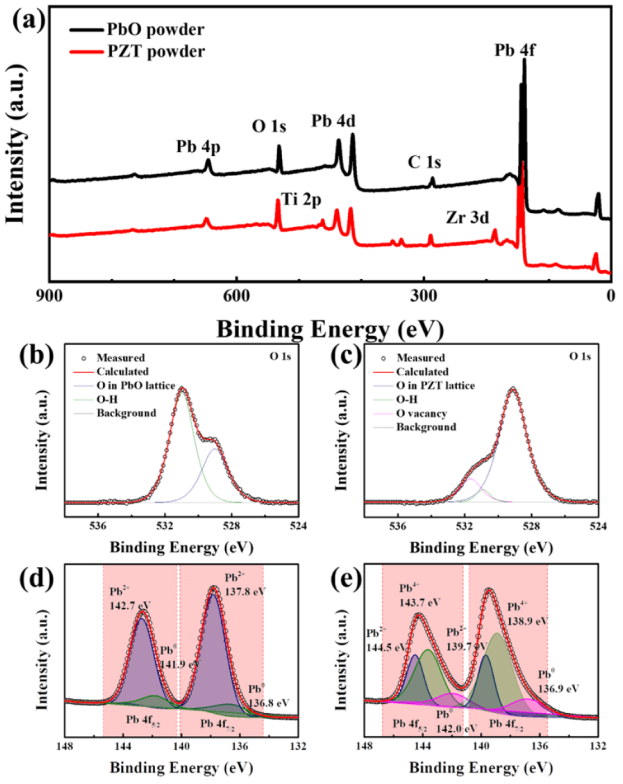

Figure 7. XPS survey spectra of (a) recycled PbO, PZT powder, and high-resolution XPS spectra of O 1s for (b) recycled PbO, (c) PZT powder, and Pb 4f for (d) recycled PbO, (e) PZT powder.

relatively dense and homogeneous microstructure with the theoretical density of the sintered sample above 95%. To assess chemical compositions following sintering, energy-dispersive spectroscopy (EDS) was used in Figure 6c, It is confirmed to contain lead (Pb), zirconium (Zr), titanium (Ti), and oxygen (O) in the sample.

Figure 7 shows XPS (X-ray Photoelectron Spectroscopy) data of recycled PbO powder and PZT powder fabricated from recycled PbO. The XPS data were calibrated using the C 1s core level peak at 284.8 eV. In the survey spectra in Figure 7a of PbO and PZT powder, core level peaks of Pb 4f, O 1s, Zr 3d, and Ti 2p can be observed.[54] The presence of a C 1s peak indicates that carbon contaminants are on the surface due to exposure to air, with no other elements found in both powders. For Figure 7b and c, the O 1s data were fitted using a Pseudo-Voigt profile under Shirley-type background conditions. The O 1s spectrum of the PbO powder is decomposed into two peaks: the PbO lattice peak at 529.0 eV and the hydroxyl oxygen peak at 530.0 eV, whereas the PZT powder shows peaks for PZT lattice, hydroxyl oxygen, and oxygen vacancy.[55] Figure 7d shows the Pb 4f spectrum of recycled PbO, with two peaks observed for both Pb 4f 7/2 and Pb 4f 5/2. Previous studies suggest that PbO peaks at 136.8 eV and Pb^{2+} peaks at 137.8 eV. The measured peaks at Pb 4f 7/2 are at 137.8 and 136.7 eV, confirming the presence of Pb^{2+} and PbO. Figure 7e presents the Pb 4f spectrum from PZT powder, where the binding energy around 136.9 eV for Pb 4f 7/2 is related to network modifiers, and the Pb ions are in states of Pb^{2+} and Pb^{4+}. The peaks between Pb 4f 7/2 and Pb 4f 5/2 are separated by a difference of 4.8 eV, resembling the "shoulder" peaks observed.[56]

Figure 8a represents the temperature dependence of dielectric constant (ε) and dielectric loss (tan δ) for the PZT sintered sample as a function of temperature at elevated temperatures. Figure 7a further plots the ε_r and tan δ variations with temperature at different frequencies of 1 kHz, 10 kHz, and 100 kHz. In Figure 8a, the Curie temperature (T_c) for PZT is observed in the temperature range of 300 °C−310 °C. At T_c, the dielectric constant (~20,000) reaches a maximum value in the PZT sintered at 1200 °C and decreases significantly at higher temperatures. Such a response characterizes the ferroelectric nature of PZT below T_c, where increases in temperature lead to an increase in the dielectric constant. Above T_c, the transition into a paraelectric phase occurs for PZT, so the dielectric constant decreases with an increase in temperature. PZT has experienced a structural phase transition from rhombohedral and tetragonal to cubic across this boundary of T_c. The dielectric permittivity at high temperatures deviates from the Curie−Weiss law while the temperature T_m corresponding to maximum is approached from higher temperatures.

$$1/\varepsilon = 1/\varepsilon_m = (T - T_m)\gamma/C \quad (1)$$

Where C represents a material-specific constant, ε = dielectric constant, $\varepsilon T_m = \varepsilon_0$; ε_m = maximum dielectric constant, γ represents the degree of diffuseness. The parameter γ indicates the degree of diffuseness in the phase transition. Figure 8b shows the calculated γ for PZT, determined from the slope, revealing a diffuse phase transition. This transition is calculated using eq 1 and is likely influenced by the presence of cations that introduce structural heterogeneities. For the sintered PZT sample, γ is measured at 1.66, indicating a predominantly ferroelectric behavior.

The dielectric constant (ε) and dielectric loss (tan δ) as a function of frequency of the PZT sintered sample is shown in Figure 8c at high temperature. It has been discovered that when frequency increases, the dielectric constant, and the dielectric loss both drop and exhibit a typical characteristic of normal dielectrics. It may be seen that when frequency increases, dielectric loss generally reduces. The reduction in dielectric constant stems from space charge polarization, a consequence of the presence of the space charge phenomenon. Nevertheless, with increasing frequencies, the supplementary dielectric loss remains relatively consistent, owing to the frequency-independent correlation observed at higher frequencies attributed to dielectric dispersion. Lower frequency measurements reveal relatively minor dielectric losses, which may be caused by both space charge polarization and structural inhomogeneity. The obtained dielectric and piezoelectric properties of the sample are discussed in Table 3. The density of the sample was measured using Archimedes principle which was 7.787 g/cm^3.

Figure 8d depicts the impedance and frequency curve of PZT ceramics. The overall system resistance is referred to as the system's impedance. The resistance's magnitude (Z') is decreasing as frequency increases. The observation shows that the compound's ac conductivity increases as frequency increases. Higher frequencies may have resulted in a reduction in the compound barrier qualities. Due to the high impedance of the materials, space charges are not responsive to applied electric fields at lower frequencies.[57] Figure 8e shows the impedance vs frequency of the PZT. It was observed that the resonance and antiresonance frequency emerged in the range of ~222−227 kHz (f_r ~ 226.4 kHz and f_a ~ 222.8 kHz).

https://doi.org/10.1021/acsomega.5c00071
ACS Omega 2025, 10, 38385−38396

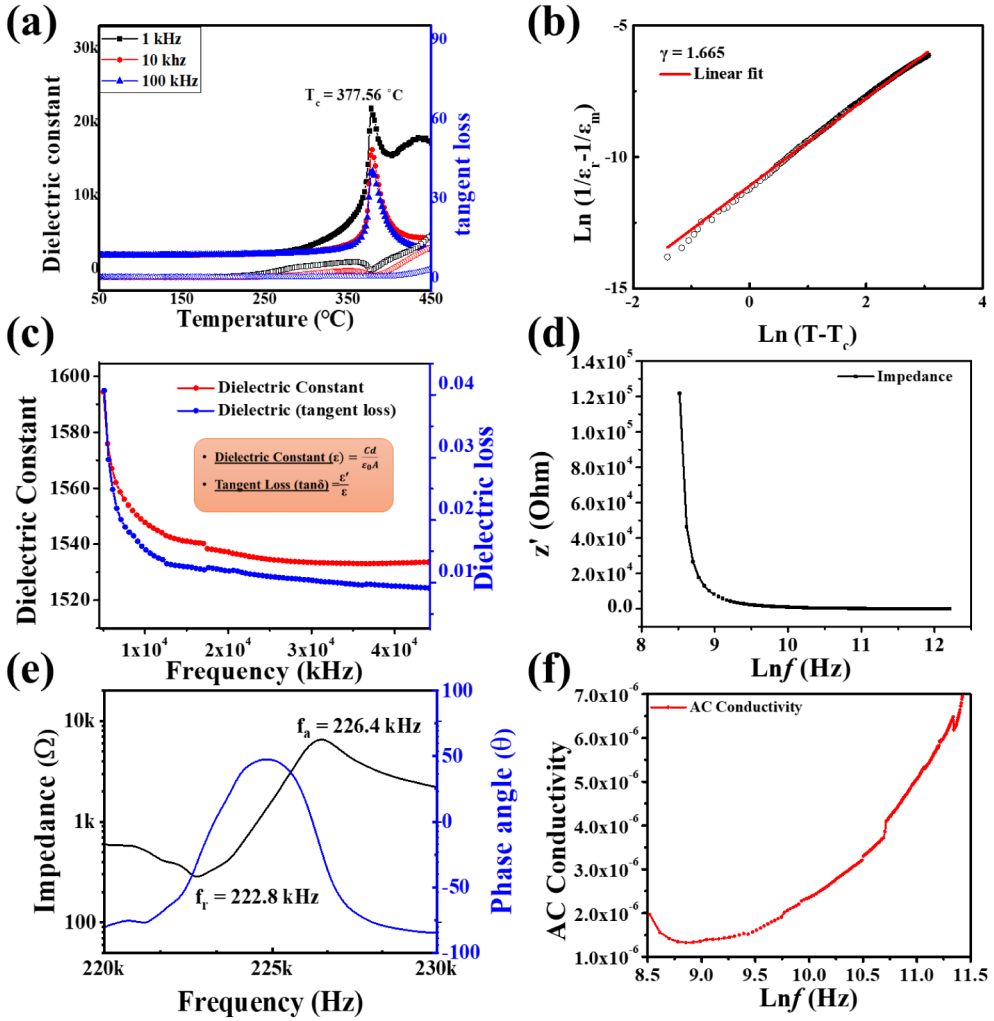

Figure 8. Dielectric and impedance characterization of the PZT sample: (a) Temperature-dependent dielectric constant and tangent loss measured at 1 kHz (black), 10 kHz (blue), and 100 kHz (red). (b) Plot of $\ln(1/\varepsilon_r - 1/\varepsilon_m)$ as a function of $\ln(T - T_m)$ of PZT. (c) Frequency-dependent dielectric constant and loss tangent. (d, e, f) Impedance magnitude and phase angle; and phase angle variation with frequency indicating dielectric relaxation. (f) AC conductivity and frequency of PZT pellets.

Table 3. Dielectric and Piezoelectric Properties of PZT Ceramic Samples

Diameter (mm)	10.26 mm
Thickness (mm)	1.06 mm
Density	7.787 g/cm^3
C_s	1.09 nF
Z_m	15 Ω
f_r	222.8 kHz
f_a	226.4 kHz
k_{31}	0.178
Q_m	30.94
d_{33}	270 pC/N
P_s	4.3 μC/cm^2
ε_c	0.94 kV/mm
P_r	1.6 μC/cm^2

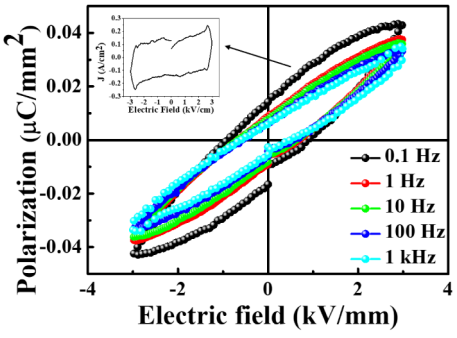

Figure 9. Polarization versus electric field (P–E loop) plot illustrating the hysteresis behavior of the material.

Figure 8f shows the frequency that promotes the ac conductivity. Frequency-dependent ac conductivity is due to the charge carriers' hopping process, which increases conductivity as frequency increases. The Koops model was used to explain why AC increases with frequency.[58,59] This model predicts that PZT material will have less conductivity at lower frequencies. The development of potential barriers at the grain borders, which prevent the movement of charge carriers from one grain to another, may be the cause of the reduced hopping mechanism that causes the conductivity to drop at lower frequencies. According to the Maxwell–Wagner model, charge carriers' behavior.[58,59]

The dielectric behavior observed in the PZT ceramic is closely linked to its structural characteristics. XRD patterns and

https://doi.org/10.1021/acsomega.5c00071
ACS Omega 2025, 10, 38385−38396

Table 4. Summarize the Dielectric and Piezoelectric Properties of Various Compositions of PZT Ceramic

Materials	d_{33} (pC/N)	P_r (μC/cm^2)	P_{max} (μC/cm^2)	E_c (kV/cm)	ε_r	k_p	T_c	ref
$Pb(Ni1/3Nb2/3)O_3$–$Pb(Zr_{0.32}Ti_{0.68})O_3$ + 0.6 wt % Sm_2O_3	738	13.03	-	2.8	6637	0.53	135	60
$Pb(Ni1/3Nb2/3)_{0.5}(Ti_{0.7}Zr_{0.3})_{0.5}O_3$	708	25.31	-	4	5770	0.59	-	61
$0.36BiScO_3$–$0.64PbTiO_3$	452	38	-	15	1455	0.52	400	62
$0.955Pb(Zn1/3Nb2/3)O_3$–$0.045PbTiO_3$	468	17.4	20.1	36.5	5132	-	263	63
$0.955Pb(Mg1/3Nb2/3)O_3$–$0.045PbTiO_3$	324	5.8	7.6	10.5	6043	-	412	63
$0.462Pb(Zn1/3Nb2/3)O_3$–$0.308Pb(Mg1/3Nb2/3)O_3$–$0.23PbTiO_3$	376	3.35	8.72	5.92	1925	-	318	63
$0.49Pb[(Zn,Ni)Nb]O_3$–$0.19Pb[(In,Yb)Nb]O_3$–$0.32Pb(Zr,Hf,Ti)O_3$	761	41.3	-	8	4557	0.63	169	64
$0.58Pb(Zr_{0.41}Ti_{0.59})O_3$–$0.42Pb(Zn_{0.4}Na_{0.6})1/3Nb_{2/3}O_3$	825	37	41	7	3603	0.7	-	65
$0.51Pb(Hf_{0.35}Ti_{0.65})O_3$–$0.49Pb(Nb_{2/3}Ni_{1/3})O_3$	1124	20	32	5	7113	0.62	133	66
$0.65Pb(Mg1/3Nb2/3)O_3$–$0.35PbTiO_3$	452	4.96	-	4.93	20311	-	175	67
$0.55Pb(Ni1/3Nb2/3)O_3$–$0.135PbZrO_3$–$0.315PbTiO_3$ (PNN–PZT)	986	21.69	-	3.22	9015	0.63	120	68
PMN-29PT + x mol % Nd_2O_3 (x = 0.02)	1230	32	37	3	6849	-	89	69
Sm-doped 0.15PMN–0.42PZ–0.43PT	-	36	40	12	2780	-	298	70
$0.05Pb(Mg1/3Nb2/3)O_3$–$0.5Pb(Mn_{1/3}Sb_{2/3})O_3$–$0.9Pb_{0.95}Sr_{0.05}(Zr_{0.48}Ti_{0.52})O_3$	348	9	23	13	1795	0.53	270	71
$0.49Pb(Ni1/3Nb2/3)O_3$–$0.2Pb(In1/2Nb1/2)O_3$–$0.31PbTiO_3$ + x mol % $LiNbO_3$ (x = 1.8)	1112	33	42	4	12092	0.53	107	72
$0.69Pb(Mg1/3Nb2/3)O_3$–$0.31PbTiO_3$ + x mol % Eu_2O_3 (x = 1)	770	30.7	-	5.3	3700	0.76 (k33)	127	73
$0.71Pb(Mg1/3Nb2/3)O_3$–$0.29PbTiO_3$ + x mol % Eu_2O_3 (x = 2)	1200	27.1	-	3.6	7870	0.77 (k33)	98	73
$0.72Pb(Mg1/3Nb2/3)O_3$–$0.28PbTiO_3$ + x mol % Eu_2O_3 (x = 2.5)	1420	22.1	-	3.5	12200	0.78 (k33)	83	73
$0.73Pb(Mg1/3Nb2/3)O_3$–$0.27PbTiO_3$ + x mol % Eu_2O_3 (x = 3)	1250	18.8	-	2.3	13520	0.64 (k33)	73	73
$Pb(Ni1/3Nb2/3)0.5(Zr_xTi_y)0.5O_3$ + 0.4 mol % Ce	700	18.24	23	4.9	5300	0.62	127	74
$Pb(Ni1/3Nb2/3)0.5(Zr_xTi_y)0.5O_3$ + 0.4 mol % Sm	620	16.6	22	4.8	5650	0.56	151	74
PMINT42/26/32	260	28	40	23	1700	-	264	75
PMINT42/26/32 − 1La4Sr	564	2.5	24	2	1900	-	265	75
PMINT42/24/35 + 1.5% Eu	462	35.09	31.92	21.34	3700	-	170	76
$0.74PbTiO_3$–0.26 $Bi(Zn2/3Nb1/3)O_3$	409	26.7	40	15.9	7500	-	467	77
0.39 $Bi(Ni1/2Ti1/2)O_3$–$0.20PbZrO_3$–$0.41PbTiO_3$	496	23.47	26.46	16.13	900	-	290	78
0.39BNT–0.20PZ–0.41PT	500	22.25	27	16	800	-	293	79
$24Pb(In_{0.5}Nb_{0.5})O_3$–$42Pb(Mg_{0.335}Nb_{0.665})O_3$–$34PbTiO_3$ + 2 mol % Sm^{3+}	420	15.18	19	13.54	2100	-	150	80
0.39 $Bi(Ni_{0.5}Ti_{0.5})O_3$–$0.20PbZrO_3$–$0.41PbTiO_3$:1BiPb	510	25.43	29	16.13	900		290	81
PZT-5A	390	-	-	-	1700	0.60	150	19,82
$Pb(Zr_{0.52}TiO_{0.48})O_3$	**270**	**1.6**	**4.3**	**0.94**	**1985**	**0.20**	**307**	**This work**

Rietveld refinement in Figure 4 confirm the coexistence of rhombohedral and tetragonal phases, indicating that the material composition lies near the morphotropic phase boundary (MPB). Raman spectroscopy further supports the presence of dual-phase coexistence with no evidence of monoclinic distortion, which facilitates easy domain wall motion and polarization switching. This structural configuration enhances the dielectric constant by enabling higher domain activity and polarization under an external electric field. Furthermore, the density and absence of secondary phases contribute to low dielectric loss. The observed diffuse phase transition behavior, with a γ value of 1.66, is attributed to slight structural disorder and phase coexistence, which is typical in MPB compositions and beneficial for broad-temperature dielectric stability.

Hysteresis loops of sample pellets were generated, poling at 3 kV/mm at 120 °C, and subsequent characterization of their ferroelectric properties. In Figure 9, the P–E hysteresis loop sample pellets were made, sintered at a temperature of 1200 °C, and poled at 3 kV/mm at 120 °C, and their characteristics were examined. Although the loops exhibit ferroelectric behavior, they do not display full saturation, which is a common challenge observed in recycled PZT ceramics and differs from typical commercial PZT behavior.[60] Table 4 summarizes the dielectric and piezoelectric properties of various compositions of PZT ceramic.

Figure 9 shows the polarization–electric field (P–E) hysteresis loop of the piezoelectric ceramics. The P–E hysteresis loop was measured at room temperature using an electric field of 3 kV/mm at frequencies of 0.1, 1, 10, 100 Hz, and 1 kHz. The piezoelectric ceramics have narrow hysteresis loops, indicating the typical PZT piezoelectric behavior. However, it should be noted that no saturation of the polarization is observed in the loops. The inset of Figure 9 demonstrates the current density versus electric field ($J - E$) and Table 3 demonstrate the dielectric and piezoelectric properties of recycled PZT ceramic samples. It should be noted that the powder exhibits a typical ferroelectric material loop and remnant polarization of 0.039 μC/mm^2. The P_r value peaked at 0.039 μC/mm^2 at 0.1 Hz and declined marginally as

https://doi.org/10.1021/acsomega.5c00071
ACS Omega 2025, 10, 38385−38396

frequency increased. The decrease of E_c can be attributed to the addition of the B-site (Zr, Ti) ions in $PbTiO_3$, which can lead to the lattice contraction and easy reversion of domains thereby decreasing E_c.

4. CONCLUSION

This study focused on environmental stewardship by developing and analyzing a soft piezoelectric PZT ceramic material, incorporating a β-PbO compound synthesized from recycled lead ingots sourced from lead-acid batteries. The emphasis was on resource recycling and environmental conservation. XRD analysis confirmed the coexistence of tetragonal and rhombohedral phases in PZT ceramic, along with the orthorhombic structure of β-PbO. The PZT sintered sample at 1200 °C has a density of 7.787 g/cm^3 with piezoelectric coefficient d_{33} of 270 pC/N, a Q_m factor of 1318, and a dielectric constant of 1590 at 10 Hz. The $P-E$ hysteresis curves revealed that the engineered PZT ceramics are soft piezoelectric materials with a high remnant polarization (P_r) and low coercive field (E_c). The findings affirm the viability of utilizing lead ingots from recycled lead-acid batteries as a PbO source, offering a promising pathway for synthesizing PZT materials with enhanced dielectric and piezoelectric properties.

AUTHOR INFORMATION

Corresponding Authors

Mohsin Saleem − *School of Chemical and Materials Engineering (SCME), National University of Sciences & Technology (NUST), Islamabad 44000, Pakistan;* orcid.org/0000-0002-6456-2323; Email: mohsin.saleem@scme.nust.edu.pk

Jung-Hyuk Koh − *School of Electrical and Electronic Engineering, Chung-Ang University, Seoul 06974, Republic of Korea; Graduate School of Intelligent Energy and Industry, Chung-Ang University, Seoul 06974, Republic of Korea;* Email: jhkoh@cau.ac.kr

Authors

Amna Idrees − *School of Chemical and Materials Engineering (SCME), National University of Sciences & Technology (NUST), Islamabad 44000, Pakistan*

Gwangseop Lee − *School of Electrical and Electronic Engineering, Chung-Ang University, Seoul 06974, Republic of Korea; Graduate School of Intelligent Energy and Industry, Chung-Ang University, Seoul 06974, Republic of Korea*

Hamid Jabbar − *Department of Mechatronics Engineering, College of Electrical and Mechanical Engineering, National University of Sciences and Technology (NUST), Islamabad 44000, Pakistan*

Muhammad Siyar − *School of Chemical and Materials Engineering (SCME), National University of Sciences & Technology (NUST), Islamabad 44000, Pakistan;* orcid.org/0000-0002-7025-217X

Muhammad Zubair Khan − *Department of Materials Science & Engineering, Pak-Austria Fachhochschule: Institute of Applied Sciences and Technology, Haripur 22621, Pakistan;* orcid.org/0009-0003-1817-2003

Farah Mumtaz − *School of Chemical and Materials Engineering (SCME), National University of Sciences & Technology (NUST), Islamabad 44000, Pakistan*

Aqeel Ahmad Taimoor − *Department of Chemical and Materials Engineering, Faculty of Engineering, King Abdulaziz University, Jaddah 21589, Saudi Arabia*

Awais Ahmad − *Department of Chemistry, The University of Lahore, Lahore 54590, Pakistan*

Tauseef Ahmed − *Interdisciplinary Research Center for Hydrogen Technologies & Carbon Management (IRC-HTCM), King Fahd University of Petroleum and Minerals, Dhahran 31261, Kingdom of Saudi Arabia*

Complete contact information is available at: https://pubs.acs.org/10.1021/acsomega.5c00071

Author Contributions

◆A.I. and G.L. have contributed equally to this work. A.I., G.L., H.J., M.Z.K., J.H.K., and M.S. conceptualized the study. F.M., A.A.T., R.A.M., M.S., G.L.F.A., and M.Z.K. characterized and analyzed the samples. A.I., G.L., A.A., and T.A. did the writing and characterizations. A.I., G.L., and H.J. carried out the measurement. G.L., M.S., R.A.M., A.A., and A.A.T. conducted the dielectric and electrical experiment. J.H.K., M.Z.K., M.A.A.T., and M.S. commented on the manuscript. All the authors discussed the results and contributed to the manuscript preparation.

Notes

The authors declare no competing financial interest.

ACKNOWLEDGMENTS

This work was jointly supported by the National Research Program of Universities (NRPU), the Higher Education Commission (HEC), Pakistan research fund "Development of lab/pilot scale facilities for the production of piezoelectric material for multilayer energy devices" 20-15673/NRPU/R&D/HEC/2021, and MSIT (Ministry of Science and ICT), Korea, under the ITRC (Information Technology Research Centre) support program (IITP-2025-RS-2020-II201655, 50%) supervised by the IITP (Institute of Information and Communications Technology Planning and Evaluation).

REFERENCES

(1) Maiti, S.; et al. Bio-waste onion skin as an innovative nature-driven piezoelectric material with high energy conversion efficiency. *Nano Energy* **2017**, *42*, 282−293.

(2) Ali, M.; Saleem, M.; Sattar, T.; Khan, M.Z.; Koh, J.H.; Gohar, O.; Hussain, I.; Zhang, Y.; Hanif, M.B.; Ali, G.; et al. High-entropy battery materials: Revolutionizing energy storage with structural complexity and entropy-driven stabilization. *Mater. Sci. Eng. R: Rep.* **2025**, *163*, 100921.

(3) Hanif, M.B.; Rauf, S.; Khan, M.Z.; Babar, Z.U.D.; Gohar, O.; Saleem, M.; Zheng, K.; Hussain, I.; Lin, B.; Medvedev, D.; et al. Innovative advances and challenges in solid oxide electrolysis cells: Exploring surface segregation dynamics in perovskite electrodes. *Mater. Sci. Eng. R: Rep.* **2024**, *161*, 100864.

(4) Kumar, C.; et al. Bio-waste polymer hybrid as induced piezoelectric material with high energy harvesting efficiency. *Compos. Commun.* **2019**, *11*, 56−61.

(5) Sanchez-Duenas, L.; Gomez, E.; Larrañaga, M.; Blanco, M.; Goitandia, A. M.; Aranzabe, E.; Vilas-Vilela, J. L. A Review on Sustainable Inks for Printed Electronics: Materials for Conductive, Dielectric and Piezoelectric Sustainable Inks. *Materials* **2023**, *16* (11), 3940.

(6) Jaffe, B.; Cook, W. R.; Jaffe, H. Piezolectric ceramics. *J. Am. Ceram. Soc.* **1971**, *41*, 494−498.

(7) Rödel, J.; Jo, W.; Seifert, K.T.; Anton, E.M.; Granzow, T.; Damjanovic, D. Perspective on the Development of Lead-Free Piezoceramics. *J. Am. Ceram. Soc.* **2009**, *92*, 1153−1177.

(8) Rödel, J.; et al. Transferring lead-free piezoelectric ceramics into application. *J. Eur. Ceram. Soc.* **2015**, *35* (6), 1659−1681.

(9) Seymour, C. L.; Gillson, L.; Child, M. F.; Tolley, K. A.; Curie, J. C.; da Silva, J. M.; Alexander, G. J.; Anderson, P.; Downs, C. T.; Egoh, B. N.; et al. Horizon scanning for South African biodiversity: A need for social engagement as well as science. *Ambio* **2020**, *49* (6), 1211−1221.
(10) Wu, A.; et al. Sol−Gel Preparation of Lead Zirconate Titanate Powders and Ceramics: Effect of Alkoxide Stabilizers and Lead Precursors. *J. Am. Ceram. Soc.* **2000**, *83*, 1379.
(11) Finger, L. W. Physical Properties of Crystals, Their Representation by Tensors and Matrices. Eos. *Trans., Am. Geophys. Union* **1983**, *64* (45), 643−643.
(12) Keve, E. T.; Bye, K. L. Phase identification and domain structure in PLZT ceramics. *J. Appl. Phys.* **1975**, *46* (2), 810−818.
(13) Haertling, G. H.; Land, C. E. Hot-Pressed (Pb,La)(Zr,Ti)O3 Ferroelectric Ceramics for Electrooptic Applications. *J. Am. Ceram. Soc.* **1971**, *54* (1), 1−11.
(14) Bobnar, V.; Kutnjak, Z.; Levstik, A. Glassy to inhomogeneous-ferroelectric crossover in (Pb,La)(Zr,Ti)O3 ceramics. *Appl. Phys. Lett.* **2000**, *76* (19), 2773−2775.
(15) Wu, J.; Xiao, D.; Zhu, J. Potassium−Sodium Niobate Lead-Free Piezoelectric Materials: Past, Present, and Future of Phase Boundaries. *Chem. Rev.* **2015**, *115* (7), 2559−2595.
(16) Maeder, M. D.; Damjanovic, D.; Setter, N. Lead Free Piezoelectric Materials. *J. Electroceram.* **2004**, *13* (1), 385−392.
(17) Lines, M. E. *Principles and applications of ferroelectrics and related materials/by M. E. Lines and A. M. Glass. The International series of monographs on physics, ed. A.M. Glass*; Clarendon Press, 1977.
(18) Shirane, G.; Suzuki, K.; Takeda, A. Phase Transitions in Solid Solutions of PbZrO3 and PbTiO3 (II) X-ray Study. *J. Phys. Soc. Jpn.* **1952**, *7* (1), 12−18.
(19) Haertling, G. H. Ferroelectric Ceramics: History and Technology. *J. Am. Ceram. Soc.* **1999**, *82* (4), 797−818.
(20) Su, B.; Ponton, C. B.; Button, T. W. Hydrothermal and electrophoretic deposition of lead zirconate titanate (PZT) films. *J. Eur. Ceram. Soc.* **2001**, *21* (10), 1539−1542.
(21) Lal, R.; Krishnan, R.; Ramakrishnan, P. Preparation and characterization of submicron reactive PZT powders. *Mater. Sci. Eng.* **1987**, *96* (C), L25−L29.
(22) Saleem, M.; et al. Large signal electrical property of CuO-doped of a Bi 0.5 Na 0.5 TiO 3−SrTiO 3. *J. Electroceram.* **2018**, *40*, 88−98.
(23) Branković, Z.; et al. Mechanochemical synthesis of PZT powders. *Mater. Sci. Eng., A* **2003**, *345* (1−2), 243−248.
(24) Zahra, N.; Shahbaz, M.; Saleem, M.; Khan, M.Z.; Irshad, M.; Sharif, S.; Koh, J.H.; Marwat, M.A.; Lee, G.; Irfan, M.; Ghaffar, A; et al. Innovative multiphase composites of transition metal oxides for long-term stability and high energy density in storage devices. *Mater. Today Sustainab.* **2025**, *30*, 101099.
(25) Saleem, M.; et al. Percolation phenomena of dielectric permittivity of a microwave-sintered BaTiO3−Ag nanocomposite for high energy capacitor. *J. Alloys Compd.* **2020**, *822*, 153525.
(26) Singh, A. P.; et al. Low-temperature synthesis of chemically homogeneous lead zirconate titanate (PZT) powders by a semi-wet method. *J. Mater. Sci.* **1993**, *28* (18), 5050−5055.
(27) Wang, S. F.; et al. Characterization of hydrothermally synthesized lead zirconate titanate (PZT) ceramics. *Mater. Chem. Phys.* **2004**, *87* (1), 53−58.
(28) Saleem, M.; Hwan, L. D.; Kim, I.-S.; Kim, M.-S.; Maqbool, A.; Nisar, U.; Pervez, S. A.; Farooq, U.; Farooq, M. U.; Khalil, H. M. W.; et al. Revealing of core shell effect on frequency-dependent properties of Bi-based relaxor/ferroelectric ceramic composites. *Sci. Rep.* **2018**, *8* (1), 14146.
(29) Saleem, M.; et al. Synthesis, sintering and dielectric properties of a BaTiO3−Ni composite. *Ceram. Int.* **2014**, *40* (5), 7329−7335.
(30) Habib, M. S.; et al. Experimental determination of electrophoretic deposition parameters and electrical characterization for K 0.5 Na 0.5 NbO3 perovskite thick films for energy harvesting applications. *Mater. Chem. Phys.* **2024**, *316*, 129074.
(31) Lim, D.-H.; et al. Frequency dependence of polarization and strain in Bi0. 5Na0. 5TiO3-SrTiO3/Bi0. 5 (Na0. 8K0. 2) 0.5 TiO3 composites. *Sens. Actuators, A* **2018**, *282*, 163−173.
(32) Koo, B.-K.; et al. Fabrication of borosilicate-glass-coated CuAg inner electrode for multilayer ceramic actuator. *Sens. Actuators, A* **2018**, *277*, 8−17.
(33) Jeong, S.-J.; et al. Temperature dependence of polarization and strain of bismuth-based ceramic composites. *J. Electroceram.* **2014**, *33* (3−4), 230−238.
(34) Jeong, S.-J.; et al. Comparative study of the polarization and strain of inclusion-type and layer-type 0.94 Bi (NaK) TiO3−0.06 BiAlO3/Bi (NaK) TiO3 ceramic composites. *J. Alloys Compd.* **2015**, *646*, 1058−1067.
(35) Hussain, M. A.; et al. Influence of spark plasma sintering temperature and hydroxyapatite nanoparticles on properties of HA based functionally graded materials for bone prosthesis. *Ceram. Int.* **2022**, *48* (10), 14481−14490.
(36) Anandakrishnan, S. S.; et al. Recycling hazardous and energy-demanding piezoelectric ceramics using an oxide−halide perovskite upside-down composite method††Electronic supplementary information (ESI) available. *See RSC Sustainability* **2024**, *2* (4), 961−974.
(37) Ranjbar, Z. R.; Morsali, A. Sonochemical syntheses of a new nano-sized porous lead(II) coordination polymer as precursor for preparation of lead(II) oxide nanoparticles. *J. Mol. Struct.* **2009**, *936*, 206−212.
(38) Shin, H.-J.; Min, B.-K. Direct Synthesis of PbO Nanoparticles from a Lead(II) Nanoflower Coordination Polymer Precursor: Synthesis, Crystal Structure and DFT Calculations of [Pb(pcih)-N3H2O]nwith the Terminal Azide Unit. *J. Inorg. Organomet. Polym. Mater.* **2013**, *23* (6), 1305−1312.
(39) Chen, X.; Chen, S.; Clequin, P.-M.; Shoulders, W. T.; Gaume, R. Combustion synthesis of lead oxide nanopowders for the preparation of PMN−PT transparent ceramics. *Ceram. Int.* **2015**, *41* (1), 755−760.
(40) Morozov, I. G.; Belousova, O. V.; Kuznetsov, M. V. High-temperature ferromagnetism and super-high-temperature superconductivity in Pb-O nanoparticles. *Mater. Sci. Eng. B* **2021**, *264*, 114940.
(41) Zhu, X.; et al. Preparation of basic lead oxide from spent lead acid battery paste via chemical conversion. *Hydrometallurgy* **2012**, *117−118*, 24−31.
(42) Zhan, L., et al. *Preparing lead oxide nanoparticles from waste electric and electronic equipment by high temperature oxidation-evaporation and condensation.*; Powder Technology: 2017, *308*, 30−36. .
(43) Alagar, M.; Thirugnanasambandan, T.; Raja, A. Chemical Synthesis of Nano-Sized particles of Lead Oxide and their Characterization Studies. *arXiv*, **2012**.
(44) Salavati-Niasari, M.; Mohandes, F.; Davar, F. Preparation of PbO nanocrystals via decomposition of lead oxalate. *Polyhedron* **2009**, *28* (11), 2263−2267.
(45) Haseeb, M.; et al. Effect of sintering temperature on microstructure, optical and dielectric properties in a low radio frequency range of a BaO: ZnO composite. *Ceram. Int.* **2023**, *49* (21), 33445−33458.
(46) Elawam, S. A.; et al. Characterizations of Beta-lead Oxide Massicot Nano-Particles. *Curr. J. Appl. Sci. Technol.* **2016**, *17* (1), 1−10.
(47) Yousefi, R.; et al. Synthesis and characterization of single crystal PbO nanoparticles in a gelatin medium. *Ceram. Int.* **2014**, *40* (8), 11699−11703.
(48) Srivastava, G.; Tiwari, V. Structural, dielectric and piezoelectric properties of 0−3 PZT/PVDF composites. *Ceram. Int.* **2015**, *41*, 8008−8013.
(49) De-Qing, Z.; Da-Wei, W.; Jie, Y.; Quan-Liang, Z.; Zhi-Ying, W.; Mao-Sheng, C. Structural and Electrical Properties of PZT/PVDF Piezoelectric Nanocomposites Prepared by Cold-Press and Hot-Press Routes. *Chinese Phys. Lett.* **2008**, *25*, 4410.

https://doi.org/10.1021/acsomega.5c00071
ACS Omega 2025, 10, 38385−38396

(50) Maity, S. R.; et al. Composition-driven structural phase transition in ferroelectric PbZrxTi1-xO3 across the morphotropic phase boundary. *J. Solid State Chem.* **2023**, *325*, 124131.
(51) Rödel, J.; et al. Perspective on the Development of Lead-free Piezoceramics. *J. Am. Ceram. Soc.* **2009**, *92* (6), 1153−1177.
(52) Burns, G.; Scott, B. A. Raman Spectra of Polycrystalline Solids; Application to the $\mathrm{Pb}{\mathrm{Ti}}_{1\ensuremath{-}x}{\mathrm{Zr}}_{x}{\mathrm{O}}_{3}$ System. *Phys. Rev. Lett.* **1970**, *25* (17), 1191−1194.
(53) Necira, Z.; et al. Synthesis of PZT powder by conventional method at various conditions. *EPJ Web Conf.* **2012**, *29*, 00038.
(54) Zomorrodian, A.; et al. XPS oxygen line broadening in lead zirconium titanate and related materials. *Appl. Surf. Sci.* **1995**, *90* (3), 343−348.
(55) Kim, J.-N.; et al. Changes in chemical behavior of thin film lead zirconate titanate during Ar ± ion bombardment using XPS. *Appl. Surf. Sci.* **2003**, *206* (1), 119−128.
(56) Ştoflea, L. E.; et al. Selective adsorption of contaminants on Pb (Zr, Ti) O 3 surfaces shown by X-ray photoelectron spectroscopy. *J. Mater. Chem. A* **2014**, *2* (35), 14386−14392.
(57) Sebastian, M. T. *Dielectric materials for wireless communication.*; Elsevier, 2010.
(58) Koops, C. G. On the Dispersion of Resistivity and Dielectric Constant of Some Semiconductors at Audiofrequencies. *Phys. Rev.* **1951**, *83* (1), 121−124.
(59) Kharabe, R. G.; et al. Dielectric properties of mixed Li−Ni−Cd ferrites. *Smart Mater. Struct.* **2006**, *15* (2), N36.
(60) Lee, Y.; et al. Physical properties of Sm2O3 added Pb(Ni1/3Nb2/3) O3−Pb(Zr0.32Ti0.68)O3 system ceramics for piezoelectric speaker application. *Ferroelectrics* **2022**, *600* (1), 148−155.
(61) Wang, H.; et al. Preparation and characterization of Pb(Ni1/3Nb2/3)0.5(Ti0.7Zr0.3)0.5O3 functionally graded piezoelectric actuator by tape-casting process. *Ferroelectrics* **2023**, *614* (1), 127−136.
(62) Ji, J.-H.; et al. BiScO3-PbTiO3 piezoelectric ceramics with Bi excess for energy harvesting applications under high temperature. *Ceram. Int.* **2020**, *46* (4), 4104−4112.
(63) Perumal, R. N.; Athikesavan, V. Investigations on electrical and energy storage behaviour of PZN-PT, PMN-PT, PZN−PMN-PT piezoelectric solid solutions. *J. Mater. Sci.: Mater. Electron.* **2019**, *30*, 902−913.
(64) Zhang, J.; Liu, H.; Sun, S.; Liu, Y.; Gao, B.; Deng, S.; Fan, L.; Chen, J.; et al. Structure and good piezoelectric performance in the complex system of Pb[(Zn,Ni)Nb]O3−Pb[(In,Yb)Nb]O3−Pb-(Zr,Hf,Ti)O3. *J. Appl. Phys.* **2020**, *128* (2), 024101.
(65) Lee, G.-S.; et al. Investigation of the structural and piezoelectric characteristics of (1-x) Pb (Zr, Ti) O3-xPb (Zn0. 4Ni0. 6) 1/3Nb2/3O3 ceramics with R-PC-T multistructure. *J. Eur. Ceram. Soc.* **2024**, *44* (12), 7006−7017.
(66) Yan, Y.; et al. Extremely high piezoelectric properties in Pb-based ceramics through integrating phase boundary and defect engineering. *ACS Appl. Mater. Interfaces* **2021**, *13* (32), 38517−38525.
(67) Augustine, P.; et al. Stabilization heat treatment and functional response of 0.65 [Pb (Mg1/3Nb2/3) O3]-0.35 [PbTiO3]. *Ceramics. Mater. Res. Bull.* **2017**, *95*, 47−55.
(68) Gao, X.; Wu, J.; Yu, Y.; Chu, Z.; Shi, H.; Dong, S.; et al. Giant piezoelectric coefficients in relaxor piezoelectric ceramic PNN-PZT for vibration energy harvesting. *Adv. Funct. Mater.* **2018**, *28* (30), 1706895.
(69) Guo, Q.; et al. Ultrahigh electrostrictive strain and its response to mechanical loading in Nd-doped PMN-PT ceramics. *Acta Mater.* **2024**, *266*, 119695.
(70) Guo, Q.; et al. Temperature-insensitive PMN-PZ-PT ferroelectric ceramics for actuator applications. *Acta Mater.* **2021**, *211*, 116871.
(71) Qiao, P.; et al. Enhancing the piezoelectric properties and thermal stability of PMN-PMS-PSZT high-power piezoelectric ceramics through defect engineering. *J. Eur. Ceram. Soc.* **2024**, *44* (12), 6935−6947.
(72) Peng, W.; et al. Giant piezoelectricity of PNN-PIN-PT ceramics via domain engineering. *J. Eur. Ceram. Soc.* **2024**, *44* (10), 5668−5676.
(73) Guo, Q.; et al. Investigation of dielectric and piezoelectric properties in aliovalent Eu3+-modified Pb (Mg1/3Nb2/3) O3-PbTiO3 ceramics. *J. Am. Ceram. Soc.* **2019**, *102* (12), 7428−7435.
(74) Peng, G.-G.; et al. Effect of rare-earth addition on morphotropic phase boundary and relaxation behavior of the PNN-PZT ceramics. *J. Alloys Compd.* **2017**, *693*, 1250−1256.
(75) Gowthami, S.; Anandha Babu, G.; Manikandan, C.; Sarguna, R. M. Effective strategy of optimized dielectric, energy storage and piezoelectric performances in La3+and Sr2+ co-doped PIMNT 42/26/32 relaxor ferroelectric ceramics. *Mater. Sci. Semicond. Process* **2023**, *166*, 107688.
(76) Gowthami, S.; Anandha Babu, G.; Manikandan, C.; Varadarajan, E.; Sarguna, R. M.; et al. Improved piezoelectric and electric field-induced strain properties in Eu3+ modified 0.42PMN−0.26PIN−0.32PT ceramics. *Appl. Phys. A* **2023**, *129* (4), 239.
(77) Aravinthkumar, P.; Gopi, G.; Babu, G. A. Investigation on structural, dielectric, ferroelectric, and piezoelectric properties of (1 − x)PbTiO3−(x)Bi(Zn2/3Nb1/3)O3 solid solutions. *J. Mater. Sci.: Mater. Electron.* **2024**, *35* (3), 200.
(78) Bharath, S.G.; Babu, G.A.; Manikandan, C.; Varadarajan, E. Effect of excess BiO/PbO on the structural and electrical properties of ternary 0.39 Bi(NiTi)O-0.20PbZrO-0.41PbTiO ceramics. *Mater. Sci. Semicond. Process.* **2024**, *172*, 108054.
(79) Bharath, S. G.; Babu, G. A.; Manikandan, C.; Varadharajan, E.; et al. Improved piezoelectric, thermal stability, and ferroelectric properties in ternary 0.39BNT−0.20PZ−0.41PT piezoceramics via low sintering temperature. *J. Mater. Sci.: Mater. Electron.* **2023**, *34* (8), 706.
(80) Babu, G. A.; et al. Enhanced piezoelectric properties in Sm-doped 24Pb(InNb)O-42Pb(MgNb)O-34PbTiO piezoceramics. *J. Mater. Sci.: Mater. Electron.* **2021**, *32* (3), 3264−3272.
(81) Bharath, S. G.; Babu, G. A.; Manikandan, C.; Varadarajan, E.; et al. Role of Bi2O3 and PbO excess on the Di-/ferro-/piezoelectric and bi-polar strain properties in 0.39Bi(Ni0.5Ti0.5)O3−0.20PbZrO3−0.41PbTiO3 ternary ceramics near MPB. *Appl. Phys. A* **2025**, *131* (1), 58.
(82) Königsberger, M.; Pichler, B.; Hellmich, C. Micromechanics of ITZ-Aggregate Interaction in Concrete Part II: Strength Upscaling. *J. Am. Ceram. Soc* **2014**, *97* (2), 543−551.

https://doi.org/10.1021/acsomega.5c00071
ACS Omega 2025, 10, 38385−38396